Active optics modernization of the AEOS telescope

David Greenwald
The Boeing Company
535 Lipoa Parkway Suite 200
Kihei HI 96753

ABSTRACT

Since first light in 1997, the Advanced Electro-Optical System (AEOS) telescope at the Maui Space Surveillance Site has used an active system for figure control that applies forces on the primary mirror and positions the secondary mirror to minimize wavefront aberrations. Periodically a wavefront optimization loop is closed with a Shack-Hartmann WaveFront Sensor (WFS), 84 primary mirror force actuators and three secondary mirror translation actuators. This optimization loop is used with a series of stellar targets to find coefficients for each force or position in a sine and cosine of elevation model. During normal telescope operation when the WFS is not in use, this elevation angle dependant model is used to control the primary mirror forces and secondary mirror positions.

Recently the system was upgraded with new computers, electronics and algorithms. The primary goal of the upgrade was to replace obsolete and no longer maintainable hardware with secondary goals of reducing the effort required to update the wavefront model, and improving the final operational wavefront performance. This paper discusses the algorithms implemented to achieve the secondary goals and initial performance results.

In order to eliminate erroneous data from the WFS, the processing algorithms were modified to dynamically assign pixels on the WFS camera to lenslets, and closed loop tracking of the gimbal was implemented using a camera that shares the focal plane with the WFS. These changes permit the elimination of human operator review from the wavefront optimization loop. The original system collected data for either a single star or a series of stars and then replaced either the constant or the complete model at the end of a data collection session. In the revised system, each wavefront measurement is used for a Kalman update to the model. Operationally, the Kalman updates allow data to be collected intermittently as time is available between other telescope tasks. By combining the relative measurement uncertainty estimated from the high spatial frequency content of each WFS measurement with the model uncertainty to compute the contribution of each measurement to the model update, the resulting model is expected to be more accurate than models generated by the old system that assumed all star observations at a given elevation angle were equally accurate. Additionally, a control loop for modal amplitude was added to generate the force commands to each actuator in real time, mitigating the wavefront degradation due to the relatively common failure of individual force actuators.

BACKGROUND

The Advanced Electo-Optical System (AEOS) telescope primary mirror is a 23:1 aspect ratio meniscus with a hydraulic wiffle tree axial support that passively distributes the support forces uniformly among 84 points on the back surface of the mirror. A mirror position control servo system adjusts the volume of fluid in three zones of the wiffle tree to maintain the mirror position in tip, tilt and piston relative to the cell edge as the cell deflects due to gravity loading. A Schwesinger[1] lateral edge support system is used normal to the elevation axis of the gimbal. This lateral system uses 48 hydraulic cylinder and linkage assemblies to apply the prescribed forces in a plane centered on the edge of the mirror, and a pattern of 24 counterweights that effectively tilt the forces to be tangent to an asphere equidistant from the front and back faces of the mirror. A position control system adjusts hydraulic fluid volume to correct for cell and linkage deflection. The last two mirror degrees of freedom which are translation of the mirror parallel to the elevation axis and rotation about the optical axis are constrained by a pair of tangent arm assemblies attached to the mirror edge.

The relatively large aspect ratio of the mirror makes it susceptible to significant wavefront degradation due to small errors in the support forces. A 1 % rms error in the forces applied by the 84 actuators if it occurs in the worst spatial pattern generates 0.93 μm rms of wavefront error. Some of the forces errors are actually randomly distributed; however a number of important ones such as residual Coulomb friction in the linkages and rolling diaphragm hydraulic cylinders are correlated over the mirror by the last correction commanded by the position servo.

Additionally the mirror was polished and tested on a similar hydraulic wiffle tree that had force error which resulted in mirror figure errors. Therefore, a low speed servo controlled force actuator that can apply up to 20 % of the nominal gravity load was included at each of the 84 axial passive hydraulic supports. The secondary mirror lateral translations are servo controlled, along with focus so that the alignment between the primary and secondary mirrors is maintained as the elevation axis rotates and the telescope truss structure deflects under its own weight. These three secondary motions are treated for wavefront control much like an additional three primary mirror actuators.

The figure control system has a real time component that applies primary force and secondary position commands from a static error and mechanical flexure based model of the system, and a calibration component that develops the model. The calibration component which is the main subject of this paper uses a Shack-Hartmann WaveFront Sensor (WFS) that is mounted at one of the four bent Cassegrain positions or trunnion box ports of the telescope, along with a refractive telescope that matches the telescope F/200 output with the WFS F/13.5 input. The real time component includes additional force commands that correct for the centripetal and angular acceleration body forces that develop during tracking. The majority of the body force which must be corrected is due to the counterweights of the lateral support that generate forces on the mirror orthogonal to the acceleration of the counterweight. The commands computed from temperature measurements of the steel telescope structure to correct for differential thermal expansion between the steel structure and Zerodur® mirrors are applied by the three individual secondary mirror position controllers.

WAVEFRONT SENSOR

The WFS shown schematically in Fig. 1 incorporates a relay lens between the lenslets and the camera as well as a fiber optic reference source. The motorized stage allows the camera to be shifted to image either the telescope pupil image at the lenslets, or the Hartmann spots at the lenslet focus. Shifting the camera is used to register the spots to their source lenslets. The reference fiber provides a known wavefront (perfect other than astigmatism and spherical aberration from the beam splitter) that is used to correct for imperfections in the lenslet array and relay lens.

There are three internal calibration steps for the wavefront sensor. The first two use the reference fiber as the light source with the images of the pupil and spot planes. The last calibration uses an image of the pupil taken with starlight. For the first calibration three images are taken with the camera imaging the lenslets at best focus, and slightly out of focus on both sides as shown in Fig. 2.

The difference between the out of focus images is processed to determine the lenslet pitch and center offset. The image taken at best pupil focus is processed to estimate the expected relative illumination of the spots produced by each lenslet.

The next calibration uses a spot plane image with the reference fiber as the light source to determine expected spot positions for a known wavefront. First a grid is fit to the spot image that provides initial estimates of spot locations. Next, a peak fitting algorithm locates each spot with sub pixel accuracy. The camera images more spots than lenslets due to the change in magnification of the relay assembly which has one lens fixed to the lenslet mount and two lenses that move with the camera. Therefore cross correlation between the relative illumination of the spots estimated from the pupil plane image and the actual spots establishes the registration between the lenslets and spots

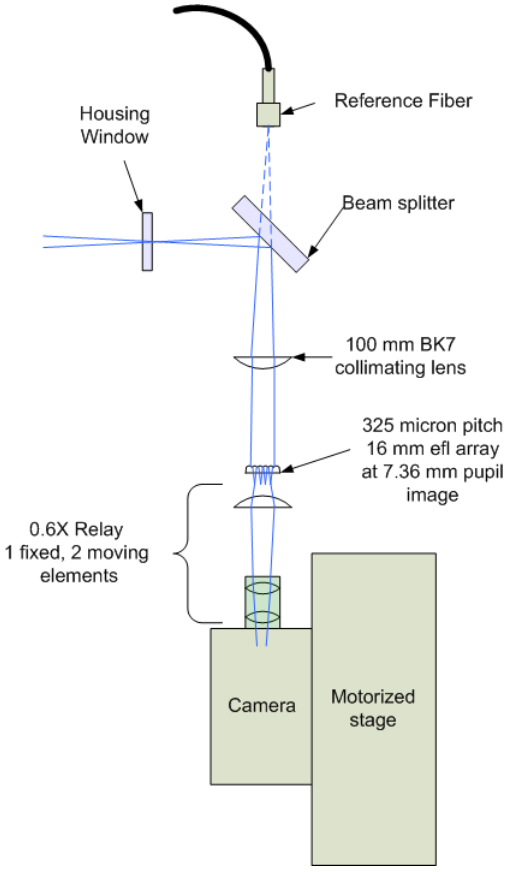

Fig. 1 WFS schematic showing the movable camera and calibration reference fiber source

identifying the extra rows and columns of spots that are from lenslets outside the pupil image. These reference spot positions will be subtracted from the spot positions of future measurements to correct for errors in the lenslet array and relay lens.

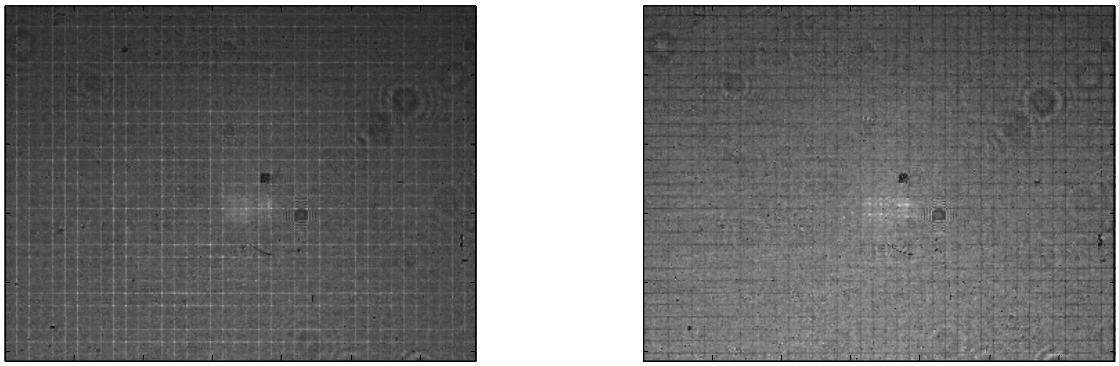

Fig. 2 Lenslet images slightly outside focus (left) showing the lenslet boundaries as a 29 x 38 grid of bright lines that nominally have double illumination, and inside focus (right) showing the lenslet boundaries as dark unilluminated lines.

The last internal calibration uses a single image of the telescope pupil to find the center location and radius of the round pupil in the image. With the lenslets located in pupil, Zernike polynomials and their gradients are computed for each lenslet center using Hedser van Brug's[2] Cartesian formulation, and the primary mirror free vibration mode gradients at each lenslet are computed from stored FEA output. The expected relative illumination from all the spots is computed along with a Boolean for each lenslet that indicates it is illuminated and has a valid reference spot offset from the prior calibration steps.

Measurements start with loop that adjusts the camera exposure until a properly exposed image is found and that image is processed. The exposure time is set so the 99.99 percentile pixel exposure is just below full well for the CCD which allows for a few "white" defective pixels in the camera. The number of pixels with an illumination that exceeds half of the peak are counted, and divided by the number of illuminated lenslets in the pupil image to estimate the spot Full Width at Half Maximum (FWHM) size.

The registration algorithm that associates spots with their sources lenslets uses Zernike polynomials in a process similar to the one Malacara-Doblado [3] discusses for primary aberrations. The first step is computing the shift in the centroid location of all the illumination between the spot and pupil images, which yields an initial estimate of the global tilt of the input wavefront. Similarly, the change in radius of gyration of the illumination patterns yields a focus estimate.

Next all the Zernike polynomials through third order are estimated based on the intensity distribution in the images. The chief ray from a lenslet located at (x_p, y_p) in the pupil plane, arrives at a point (x_s, y_s) in the spot plane, when the input wavefront aberration is described by Zernike polynomials (Z_i) with amplitudes a_i. Ignoring second and higher derivatives of the Zernike polynomials results in equations for spot locations of:

$$x_S(x_P, y_P) = x_P + EFL_{Lenslet} \sum_{i=1}^{m} a_i \frac{\partial Z_i(x_P, y_P)}{\partial x}$$

$$y_S(x_P, y_P) = y_P + EFL_{Lenslet} \sum_{i=1}^{m} a_i \frac{\partial Z_i(x_P, y_P)}{\partial y}$$

When the Zernike mapping between the pupil and spots is correct, the summation of the illumination Zernike polynomial product will match for the pupil and spot images. Therefore an error measure ε_i for each Zernike Polynomial is:

$$\varepsilon_i = \sum_{all\ j,k} \boldsymbol{I_S}(j,k) Z_i(x_s(j,k), y_s(j,k)) - \sum_{all\ j,k} \boldsymbol{I_P}(j,k) Z_i(x_P(j,k), y_P(j,k))$$

Where $\boldsymbol{I_S}(j,k)$ and $\boldsymbol{I_P}(j,k)$ are normalized image intensity in the spot and pupil planes at the j, k pixel. The normalized positions (x_p, y_p) in the pupil are computed directly from the center and diameter established based on the image. In the spot plane, (x_s, y_s) are computed from the pupil values using the equations above for the location change due to Zernike aberrations. Zernike polynomials are of course orthogonal over a circular pupil which is a reasonable approximation of $\boldsymbol{I_S}$ and $\boldsymbol{I_P}$ that allows the values of all the a's to be computed independently with a recursive implementation of Newton's method. The resulting Zernike fit is used to compute an initial estimate of each spot location in the image. These spot location estimates are correct when the wavefront can be described by Zernike polynonials through 2nd order (tilt, focus, astigmatism) and approximate for coma and trefoil.

The final spot locations are found with sub-pixel accuracy using a parabolic fit to the intensity peak. The width of the parabola is the larger of three pixels and the average Full Width at Half Maximum (FWHM) of the spots which was computed from the total number of pixels above half the maximum pixel intensity in the spot image and the number of illuminated lenslets. The peak fitting algorithm is initialized with spot location from Zernike intensity algorithm and operates recursively. If the parabola fit is a peak as determined by a negative quadratic coefficient, the peak location is updated. If the fit is a minimum, the location estimate is shifted towards the brightest pixels in the cluster being used for the fit. This process is repeated until the spot location is within half a pixel of the center of the cluster being used for the fit, or the solution is oscillating on a pixel boundary.

The reference spot locations for each lenslet which were found previously are subtracted from the measured location and the raw wavefront gradient is computed by scaling the result based on pixel size, lenslet effective focal length and magnification between the telescope aperture and lenslet array. The final gradients are computed by subtracting the gradient error due to the beamsplitter in the WFS and the refractive telescope in the optical path between the secondary mirror that generates the F/200 telescope focal plane, and WFS which has an F/13.5 input.

The beamsplitter in the WFS introduces astigmatism and spherical aberration into the wavefront, which was measured during integration of the system by shifting the reference fiber to the telescope focal plane near the window during calibration of the WFS, and then back to its normal position where it was used as the source rather than starlight. The resulting measurement yielded the Zernike polynomials for astigmatism and spherical aberration that are subtracted from the raw gradients. The refractive telescope has some residual astigmatism and coma, which was measured by inserting a beamsplitter cube near the input window to the WFS and using the reference fiber to generate outgoing illumination from the focal plane. A spherical mirror placed between the refractive telescope and the telescope secondary mirror returned the illumination back to the WFS. The WFS measurement is double the error in refractive telescope which was again fit to Zernike polynomials for correction of the gradients.

There are two validity tests; the first verifies that the relative illumination of each spot is within 50% of the expected value based on the pupil plane illumination, the second verifies the spacing to adjacent spots. The threshold for too much illumination was set at 150 % of the expected value, given that 200 % would be the result of having aberrations sufficient for two spots to overlap. The minimum illumination was set at 50 % of the expected value. The separation between adjacent spots is expected to be the lenslet pitch as modified by the low order intensity based Zernike fit. A pitch in excess of 150 % of the expected value is an indicator of having missed a spot, while a pitch less than 50 % of the expected value may indicate the same spot was measured for two adjacent lenslets. The sensor reports a measurement validity flag for each lenslet which is true if the lenslet had a valid reference spot location offset, was illuminated in the telescope pupil and has a spot illumination in the acceptable range. Additionally, if a spot separation error is found for any otherwise acceptable spot, the validity flags are set uniformly false. In simulation spot spacing errors are often found for an entire row or column of spots, with correct values reported on one side of the detected errors, and incorrect values on the other side. The test is insufficient to determine which side of the detected defect is correct; therefore all spots are reported as invalid.

WAVEFRONT OPTIMIZATION

The first step in the wavefront optimization is to convert a measured wavefront error into a force error. With approximately 350 gradient measurements and 87 actuators one could use a least squares fit of the actuator influence functions computed by Finite Element Analysis (FEA) of the primary mirror and ray tracing for secondary mirror motion, however this approach fails due to the limited force available from the primary mirror actuators. Noethe[4] suggests using minimum energy modes for correcting thin meniscus mirrors. He showed that the minimum energy modes are equivalent to the free vibration modes, and that first mode is the most compliant (largest rms deflection to rms force ratio) deflection shape, and that each mode thereafter is the most compliant orthogonal shape to the lower modes. Therefore, the minimum wavefront error is achieved by correcting modes in order until the force limit of the actuators is reached. The benefit of using the vibration modes can be seen in Fig. 3 where the response to a point load at actuator 42 is shown. The load is reacted by all 84 of the supports in the hydraulic wiffle tree, producing a wavefront error that extends over the full mirror. The fit using the modes of Fig. 4 removes over 95 % of the peak to valley error with a peak force of 13 % of the load, leaving just a small bump on the mirror surface at the load application point.

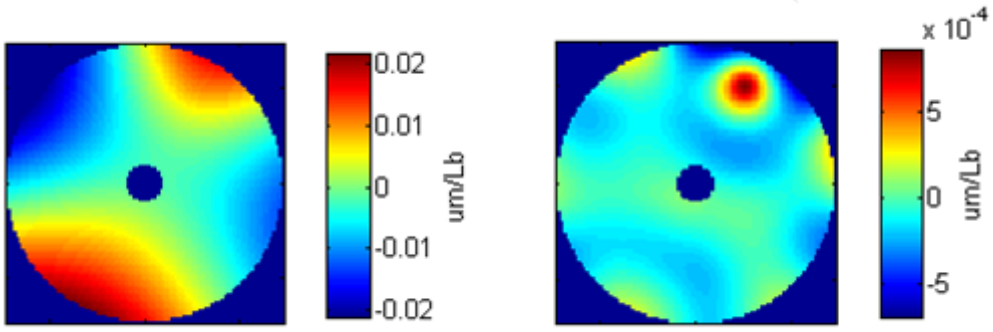

Fig. 3 Primary mirror deflection due to a point load at actuator 42 (left) and residual after 14 vibration mode fit that use 3.4 % RMS (over all actuators) of the point load to implement (right).

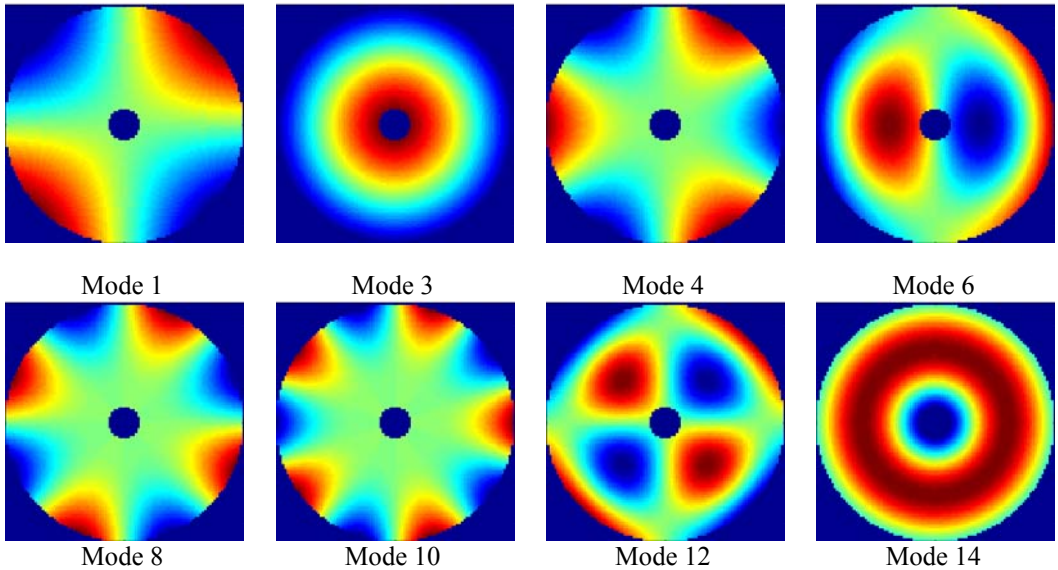

Fig. 4 Mirror mode shapes, only one of all the asymmetric pairs are shown.

Secondary mirror motion wavefront changes are not orthogonal with the mirror vibration modes, as they closely resemble modes 3 (focus), 6 and 7 (coma). Therefore, modes 3, 6 and 7 were replaced in the wavefront optimization process by Zernike polynomials for focus and coma. The higher order differences between the modes and Zernike polynomials would appear first as mode 14 which resembles spherical aberration, and is too stiff to be effectively corrected by this system.

FEA of the primary provided the first 14 non-trivial free vibration frequencies, normalized displacements and gradients on the front face, and displacements at the 84 actuators. The mode shapes and Zernike polynomials are combined into a matrix $\boldsymbol{H_{ModeToGrad}}$ that converts a column vector of mode amplitudes to gradient vectors at all the lenslets. A pseudo-inverse $\boldsymbol{H_{GradToMode}}$ converts in the opposite direction. The 84 actuators are arranged in 6 rings of 4, 8, 12, 16, 20 and 24 actuators where the inner and outer rings support 102 Lb at zenith, while the other 4 rings support 120 Lb. Using the concept of modal mass the force at each actuator required to generate a unit static deflection in the jth mode shape is computed from the mass supported by the ith actuator (M_i) the mode normalized displacement at the actuator ($z_{i,j}$) and the mode angular frequency (ω_j) to produce a matrix $\boldsymbol{H_{ModeToForce}}$ with elements:

$$H_{ModeToForce_{i,j}} = M_i \omega_j z_{i,j}^2$$

The wavefront correction model is stored as state vector ($\boldsymbol{X}$) with a length which is 3 times the number of correction modes (N_{modes}), where the states are modal amplitude coefficients of a gravity flexure model. A matrix $\boldsymbol{H_{StateToMode}}$ that converts the state vector to modal amplitudes is assembled from identity matrices of size N_{modes} and sine and cosine of the elevation angle (θ).

$$\boldsymbol{H_{StateToMode}} = [\boldsymbol{I}\sin\theta \quad \boldsymbol{I}\cos\theta \quad \boldsymbol{I}]$$

The force command vector ($\boldsymbol{F_{Cmd}}$) where the + superscript indicates the value after updating is:

$$\boldsymbol{F_{Cmd}^{+}} = \boldsymbol{H_{ModeToForce}}[\boldsymbol{H_{StateToMode}X} + K_{stuck}\boldsymbol{H_{ModeToForce}^{-1}}(\boldsymbol{F_{Cmd}} - \boldsymbol{F_{Meas}})]$$

Differences between the last force command and measured forces ($\boldsymbol{F_{Meas}}$) are converted modal amplitude via a pseudo inverse of the $\boldsymbol{H_{ModeToForce}}$ matrix, and then added to the mode command which produces an integral control loop for modal amplitude with gain K_{Stuck} that compensates for stuck force actuators.

For each star measurement the gradient vector reported by the WFS is used to compute modal amplitudes ($\boldsymbol{A_{Meas}}$) and the fit residual error ($\boldsymbol{\varepsilon_G}$).

$$\boldsymbol{A_{Meas}} = \boldsymbol{H_{GradToMode}G}$$
$$\boldsymbol{\varepsilon_G} = \boldsymbol{G} - \boldsymbol{H_{ModeToGrad}A_{Meas}}$$

The main source of error in WFS measurements is turbulence in the atmosphere, which also varies significantly between measurements. Therefore, the measurement covariance ($\boldsymbol{P_{Meas}}$) is computed from the measurements under the assumptions that the control modes are sufficient to correct the system and the residual error in fitting the gradients to the modes is all due to the atmosphere. The relationship between the fitting residual and measurement variance of the modes was found by combining the turbulence Power Spectral Density (PSD) shape of $f_s^{-8/3}$ given by Greenwood and Fried[5] where f_s is spatial frequency, with a long exposure time average PSD, and Rossing's [6] generalization of Chladni's equation for mode vibration frequencies of round plates. Fitting Rossing's equation to the FEA mode frequencies resulted in:

$$\omega_{n,m} = 15(m + 2.81n)^2$$

Where m is the number of nodes diameters in the mode, and n the number of node circles making m+2.81n a spatial wave number. This fit has a 7.0 % rms difference in frequency from the FEA results. A fit with an exponent of 1.96 has a 6.8 % rms error, but is less convenient for calculation. 18th century physicist Ernest Chladni equation for flat plates fixed at the center has a exponent of 2, and a multiplier on n of 2.

The WFS exposure time is typically 0.5 to 5 seconds which is long enough for the wind to move the atmospheric turbulence. With a frozen turbulence model of the atmosphere the number of independent realizations of turbulence

with at a give spatial frequency is proportional to the frequency, so the atmospheric contribution to the measurement error is inversely proportional to f_s. Combining these three effects yields a PSD proportional to vibration frequency to the -11/6 power. Integrating over the 15th and higher modes which are never used to correct the mirror yields the coefficient for computing the mode variance ($\sigma^2_{n,m}$) as a function of the mode frequency and measurement residual ($\sigma^2_{Residual}$).

$$\sigma^2_{n,m} = 6200Hz^{11/6}\,\omega_{n,m}^{-11/6}\,\sigma^2_{Residual}$$

$$\sigma^2_{Residual} = \frac{\boldsymbol{\varepsilon_G W_{Valid} \varepsilon_G}^T}{N_{Valid}} \frac{N_{Illum}}{N_{Valid}} + \boldsymbol{C_{Tilt} A_{Tilt}}$$

The WFS output includes a flag for each lenslet that indicates valid data; these flags are assembled onto the diagonal of the weighting matrix ($\boldsymbol{W_{Valid}}$) to eliminate invalid gradient residuals. The ratio of the number of illuminated lenslets in the pupil (N_{Illum}) to the number of valid measurements (N_{Valid}) is used to increase the measurement covariance when the WFS has rejected some spots. The mean square residual ($\sigma^2_{Residual}$) is also increased based on the measured wavefront tilt ($\boldsymbol{A_{Tilt}}$). The vector ($\boldsymbol{C_{Tilt}}$) accounts for the WFS accuracy degradation with tilt due to field aberrations in the collimating lens and relay assembly. This term was included since the star tracking when taking data can be done manually or automatically with a camera collocated with the TWF, so the operator could take data with significant tilt. The modal variances are assembled into a diagonal covariance matrix $\boldsymbol{P_{Meas}}$ with the primary mirror vibrations modes 3, 6, and 7 which were similar to focus and coma used to estimate the measurement variances associated with secondary mirror motion.

The Kalman gain matrix ($\boldsymbol{K}$) is computed from the state covariance matrix ($\mathbf{P_{States}}$), the modal amplitude measurement, measurement covariance matrix and a process noise term $\boldsymbol{Q}$ which will be discussed later. The state and state covariance update is:

$$\boldsymbol{K = P_{States} H^T_{StateToMode} \left(H_{StateToMode} P_{States} H^T_{StateToMode} + P_{Measure} \right)^{-1}}$$

$$\boldsymbol{X^+ = X + K A_{Meas}}$$

$$\boldsymbol{P_{States}{}^+ = (I - K H_{StateToMode}) P_{States}}$$

Smugness of the Kalman estimator, where the model covariance is so small that new measurements are ignored is avoided by increasing the covariance by a fraction of the measured error squared whenever the measured error squared is more than ten times the expected measurement error based on the model and measurement covariances.

The true state of the telescope wavefront changes with temperature and temperature gradients in the primary mirror. This dependence is represented statistically by the process noise $\boldsymbol{Q}$ which is estimated from the difference between states at the beginning ($\mathbf{X_{Start}}$) and of a modeling session. The difference between models which is not accounted for by the uncertainty in the models ($\boldsymbol{\Delta X^2}$) is:

$$\boldsymbol{\Delta X^2 = (X - X_{Start})(X - X_{Start})^T - P_{States} - P_{States_{Start}}}$$

There is a potential problem with negative elements on the diagonal of $\boldsymbol{\Delta x^2}$, which will happen when the change in the value of member of $\boldsymbol{X}$ is less than the uncertainty in the measurements. In this case the change can be set as zero as any actual process noise for a model element is smaller than the model uncertainty, so the model uncertainty will serve to maintain a suitable Kalman gain. This results in elements $\boldsymbol{Q_{Est}}$ and an update of $\boldsymbol{Q}$ as follows:

$$\boldsymbol{Q_{Est}}(i,j) = \begin{Bmatrix} \boldsymbol{\Delta x^2}(i,j) & \boldsymbol{\Delta x^2}(i,i) > 0 \\ 0 & \boldsymbol{\Delta x^2}(i,i) \le 0 \end{Bmatrix}$$

$$\boldsymbol{Q^+} = \left[1 - K_Q \left(1 - e^{-\Delta t/\tau}\right)\right] \boldsymbol{Q} + K_Q \boldsymbol{Q_{Est}}$$

Where K_Q is a gain of approximately 0.1, Δt is the elapsed time between models, and τ is the mirror thermal time constant. At the start of each modeling session the state covariance is updated by the process noise:

$$\boldsymbol{P}^{+}_{\boldsymbol{States}} = \boldsymbol{P}_{\boldsymbol{States}} + \boldsymbol{Q}\left(1 - e^{-\Delta t/\tau}\right)$$

Kalman estimators are typically initialized with a zero model vector and large values on the diagonal of the covariance matrix. This approach was tried during integration of the system and may have resulted in the system automatically reducing the number of control modes to minimize applied forces. If the first measurement is sufficiently noisy, the force to commands when the model is updated could exceed the capability of the actuators. A much better initialization of the system is to convert a random mean square force error based on a fraction of the actuator capacity into a mode covariance, and then assembly a state covariance. Using this approach the initial mode covariance ($\boldsymbol{P}_{\boldsymbol{States0}}$) based on the peak force available from an actuator (F_{Max}) which is assumed to be triple the rms is:

$$\boldsymbol{P}_{\boldsymbol{Modes_0}} = \boldsymbol{H}_{\boldsymbol{ForceToMode}}\boldsymbol{H}^{\boldsymbol{T}}_{\boldsymbol{ForceToMode}}\left(\frac{F_{Max}}{3}\right)^{2}$$

where $\boldsymbol{H}_{\boldsymbol{ForceToMode}}$ is a pseudo-inverse of the $\boldsymbol{H}_{\boldsymbol{ModeToForce}}$ matrix. The initial state covariance is:

$$\boldsymbol{P}_{\boldsymbol{States_0}} = \frac{1}{3}\begin{vmatrix} \boldsymbol{P}_{\boldsymbol{Modes_0}} & \boldsymbol{0} & \boldsymbol{0} \\ \boldsymbol{0} & \boldsymbol{P}_{\boldsymbol{Modes_0}} & \boldsymbol{0} \\ \boldsymbol{0} & \boldsymbol{0} & \boldsymbol{P}_{\boldsymbol{Modes_0}} \end{vmatrix}$$

INITIAL RESULTS

Several figure models have been created and updated during system integration. When used with a tracker that maintains the telescope pointing which shifts as the loop changes the secondary mirror position, the wavefront optimization loop is run for 5 or 10 cycles without any user input, and in all but three cases without error. In one case a star just a few degrees from the moon was used, and all the spots were rejected due to excessive stray light affecting the registration of spots to lenslets. In a second case a M_v 1 star was used rather than the more typical M_v 3 or 4. The WFS rejected about half the spots due to intensity mis-match presumably due to the combination of atmospheric turbulence and the short exposure time. Of more concern was the only bad series of measurements that were not detected, which were from two stars of approximately the same brightness with an 8 µrad separation. The two overlapping sets of spots were clearly visible in the spot images, but not detected by the WFS. This bad measurement happened with a new model that left the telescope sufficiently out of focus that the operator did not realize two stars where in the image from the boresight camera that shares the WFS focal plane. All the initial models have been made with at least one actuator that is stuck apparently with minimal impact on the models, even as some of the actuators would stick for a while and then start working again.

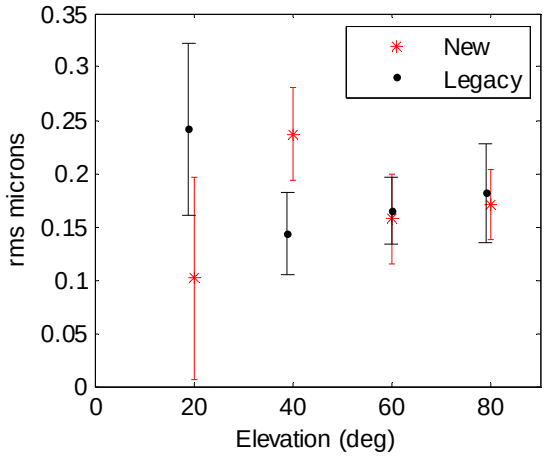

Fig. 5 Residual wavefront error in the control modes expect focus with the new and legacy models.

Fig. 5 shows the performance of a new model along with the last model created using the legacy system used since first light, and described by Kimbrell and Greenwald[7]. A series of 20 WFS measurements on each of a series of stars was collected for both systems, on two different nights. The new model was created using elevation angles less than 90 deg. due to a software bug, while the legacy model was created with stars over the 0-180 range of the telescope. Focus is not included in the reported wavefront errors. Adding more star observations to the new model which was created more to verify functionally than performance should improve the model, assuming the telescope wavefront is repeatable over time.

1 Gehard Schwesinger, *Lateral Support of Very Large Telescope Mirrors by Edge Forces Only*, J. Modern Optics, Vol. 38 No. 8, 1507-1516, 1991.
2 Hedser van Brug, *Efficient Cartesian representation of Zernike polynomial in computer memory*, SPIE Vol. 3190, 382-92, 1997.
3 Daniel Malacara-Doblado, Zacarias Malacara-Hernandez, and Armando Gomez-Yieyra, *Primary wavefront aberrations calculation from a defocused image or a Hartmanngram,* Applied Optics, Vol. 49 No. 12, 2302-2308, 2010.
4 L. Noethe, *Use of minimum-energy modes for modal-active optics corrections of thin meniscus mirrors*, J. Modern Optics, Vol. 38 No. 6, 1043-1066, 1991.
5 Darryl P. Greenwood, David L. Fried, *Power spectra requirements for wave-front-compensative systems*, JOSA Vol. 66 No. 3, 193-206, 1976.
6 Thomas D. Rossing, *Chladni's law for vibrating plates*, American J. Physics, Vol. 50 No. 3, 271-274, 1982.
7 James E. Kimbrell, David Greenwald, *AEOS 3.67m telescope primary mirror active control system*, SPIE Vol. 3352, 400-411, 1998